Nanoscale

ROYAL SOCIETY
OF CHEMISTRY

PAPER

Check for updates

View Article Online
View Journal | View Issue

Sulfonated NbS$_2$-based proton-exchange membranes for vanadium redox flow batteries†

Hossein Beydaghi, [ID] ‡[a,b] Sebastiano Bellani, [ID] ‡[b] Leyla Najafi,[b]
Reinier Oropesa-Nuñez,[c] Gabriele Bianca,[a,d] Ahmad Bagheri, [ID] [a] Irene Conticello,[b]
Beatriz Martín-García, [ID] [a] Sepideh Kashefi,[e] Michele Serri, [ID] [a] Liping Liao,[f]
Zdeněk Sofer, [ID] [f] Vittorio Pellegrini[a,b] and Francesco Bonaccorso [ID] *[a,b]

In this work, novel proton-exchange membranes (PEMs) based on sulfonated poly(ether ether ketone) (SPEEK) and two-dimensional (2D) sulfonated niobium disulphide (S-NbS$_2$) nanoflakes are synthesized by a solution-casting method and used in vanadium redox flow batteries (VRFBs). The NbS$_2$ nanoflakes are produced by liquid-phase exfoliation of their bulk counterpart and chemically functionalized with terminal sulfonate groups to improve dimensional and chemical stabilities, proton conductivity (σ) and fuel barrier properties of the as-produced membranes. The addition of S-NbS$_2$ nanoflakes to SPEEK decreases the vanadium ion permeability from 5.42×10^{-7} to 2.34×10^{-7} cm^2 min^{-1}. Meanwhile, it increases the membrane σ and selectivity up to 94.35 mS cm^{-2} and 40.32×10^4 S min cm^{-3}, respectively. The cell assembled with the optimized membrane incorporating 2.5 wt% of S-NbS$_2$ nanoflakes (SPEEK:2.5% S-NbS$_2$) exhibits high efficiency metrics, *i.e.*, coulombic efficiency between 98.7 and 99.0%, voltage efficiency between 90.2 and 73.2% and energy efficiency between 89.3 and 72.8% within the current density range of 100–300 mA cm^{-2}, delivering a maximum power density of 0.83 W cm^{-2} at a current density of 870 mA cm^{-2}. The SPEEK:2.5% S-NbS$_2$ membrane-based VRFBs show a stable behavior over 200 cycles at 200 mA cm^{-2}. This study opens up an effective avenue for the production of advanced SPEEK-based membranes for VRFBs.

[a]*Graphene Labs, Istituto Italiano di Tecnologia, via Morego 30, 16163 Genova, Italy. E-mail: Francesco.Bonaccorso@iit.it*

[b]*BeDimensional SpA, via Lungotorrente Secca 30R, 16163 Genova, Italy*

[c]*Department of Material Science and Engineering, Uppsala University, Box 534, 75103 Uppsala, Sweden*

[d]*Dipartimento di Chimica e Chimica Industriale, Università degli Studi di Genova, via Dodecaneso 31, 16146 Genoa, Italy*

[e]*Department of Chemical Engineering, Semnan University, Semnan, 3513119111, Iran*

[f]*Department of Inorganic Chemistry, University of Chemistry and Technology Prague, Technická 5, 166 28 Prague 6, Czech Republic*

†Electronic supplementary information (ESI) available. See DOI: 10.1039/d1nr07872k

‡These authors contributed equally.

1. Introduction

Major efforts are currently underway to increase the dependence on renewable energy sources (*e.g.*, wind, solar, wave, and biofuel) while limiting greenhouse gas production.[1–3] However, the storage of energy produced from renewable energy sources for use in on-demand applications is an essential requirement for achieving the transition to fossil fuel-free economies.[4] High-efficiency energy storage devices are progressively developing to meet an ever-growing energy demand with an increasing share of renewable energy sources.[5] In the class of energy storage devices, vanadium redox flow batteries (VRFBs) have attracted global research attention for their use in large-scale hybrid power systems due to their high energy efficiency (> 80% at a current density >100 mA cm^{-2}),[6] environment friendliness, and rapid response.[7–9] In VRFB systems, the proton-exchange membrane (PEM) is a crucial component that separates the electrolytes of the cathode (catholyte) and the anode (anolyte). The PEM also transports the protons to close the cell electrical circuit.[10] Standard PEMs have to fulfill concomitant characteristics, such as high proton conductivity (σ) (≥80 mS cm^{-1}), low vanadium ion permeability (P) (≤10^{-7} cm^2 min^{-1}), ability to prevent excessive water transport, low membrane swelling (MS) (≤10%), and excellent chemical and mechanical stabilities during VRFB operation.[9,11] The use of a an effective PEM is essential to realize a VRFB with high energy efficiency (EE).[12] The most popular commercial flow cell separators are Nafion membranes, which exhibit high σ (~90 mS cm^{-1} at 25 °C), as well as excellent thermal and chemical stabilities.[13,14] However, their high P (~10^{-6} cm^2 min^{-1}) and high price (~180 US$ per m^2 for Nafion 117 and an annual production of 100 000 m^2) represent limiting factors

that drive the research toward the development of more convenient alternatives.[15,16] In this context, membranes based on sulfonated poly(ether ether ketone) (SPEEK) have demonstrated great potential to replace Nafion membranes due to their superior mechanical strength (tensile strength ~37 MPa, >80% higher than that of Nafion 117),[17,18] high σ (~40 mS cm^{-1} at 25 °C), film-formation ability, optimal thermal stability (up to 300 °C) and limited P.[19–22] More in detail, in SPEEK membranes, the well-balanced hydrophilic–hydrophobic nanophase separation in the form of hydrophilic micro-domains dispersed in a hydrophobic matrix effectively prevents the permeation of vanadium species, while guaranteeing efficient proton transport.[23] However, the properties of SPEEK membranes strongly depend on the degree of sulfonation (DS), since sulfonate groups play a key role in the interconnection of ionic channels.[24] By increasing the DS, water uptake (WU) and σ increase, but MS and P can also decrease together with a worsening of the mechanical stability.[25] Therefore, it is challenging to find solutions that provide mechanically and chemically stable high-DS SPEEK-based membranes with high σ while maintaining P and MS.[26] For this purpose, many methods have been reported to fabricate nanocomposite membranes[27–31] and modify SPEEK-based PEMs, such as the incorporation of additives (e.g., graphene and its derivatives,[32,33] metal oxides,[34–36] and perovskite nanoparticles),[37] the blending with another base polymer (e.g., polybenzimidazole),[26] the functionalization with positive ionic groups (e.g., amphoteric side chains),[38] the incorporation of cross-linking agents,[39] and the design of multilayer structures.[40]

As a striking example of functional additives, two-dimensional (2D) materials have been widely used to develop nanocomposite PEMs due to a plethora of their distinctive thermal, chemical and structural properties.[41–43] Among 2D materials, transition metal dichalcogenides (TMDs), including group-6 ones (i.e., MX$_2$, in which M = Mo or W and X = S, Se or Te), have been successfully incorporated in prototypical PEM polymeric matrixes due to their facile functionalization via covalent attachment or van der Waals bonding of functional groups to metallic defects and/or polar sites (e.g., edge sites in the 2H phase of MoS$_2$).[44–48] In addition, the functionalization of group-6 TMDs can also rely on the electron transfer between electron-rich metallic phases (e.g., 1T in MoS$_2$) and reactant precursors.[49,50] Based on this last consideration, we have recently reported that group-5 TMDs (in which M = Ta, Nb or V) can be effectively functionalized with sulfonate groups (–SO$_3$H)[49] owing to the metallic character of their natural stable phases,[50–52] including several polytypes (e.g., depending on the specific material, 2H,[53,54] 3R,[55] 6R,[56] and 1T).[57,58] The functionalization of metallic TMDs with sulfonate groups can speed up the proton transport through interconnected hydrophilic channels in the membrane, thus increasing the σ of the hosting polymeric matrix.[52,59] More specifically, sulfonate groups play a significant role in both the main proton transfer mechanisms of PEMs, i.e., vehicle and Grotthuss mechanisms.[60,61] Like other 2D materials,[62,63] the morphology of group-5 TMDs can act as a barrier against the diffusion of

vanadium species into the hosting polymer matrix by increasing the transport channel tortuosity.[32] Ions with large hydrated radii (V^{n+}) can be blocked by the sheet-like structure of the nanoflakes, while small ions like H$^+$ can permeate through the interlayer spacing between the nanoflakes.[64] This effect can decrease the P of high-DS PEMs with high σ,[42,52] boosting both the coulombic efficiency (CE) and the voltage efficiency (VE) of the resulting VRFBs.[65,66] It is noteworthy that the hydrogen bonds formed between the functional groups of the sulfonated TMD nanoflakes and the polymer regulate the hydrophobic/hydrophilic nanophase separation, leading to high membrane selectivity.[67,68] Meanwhile, functional sulfonate groups allow functionalized TMDs to be homogeneously dispersed in polar solvents that are commonly used to process PEM polymers,[23] facilitating the preparation of nanocomposites. The strong hydrogen bonding between the sulfonate groups of TMD nanoflakes and polymer chains compacts the membrane structure, improving the dimensional stability of the membranes.[32,69] The thermal and chemical properties of TMD nanoflakes can also positively influence the thermo-chemical stability of the nanocomposite membranes, which must tolerate oxidative VO$_2^+$ catholytes.[70,71]

Herein, we report the synthesis of novel PEMs for VRFBs based on SPEEK and functionalized niobium disulphide (S-NbS$_2$) nanoflakes via a solution casting method. The nanocomposite PEMs have high σ (94.35 mS cm^{-1}), low P (2.34 × 10^{-7} cm^2 min^{-1}) and excellent selectivity (40.32 × 10^4 S min cm^{-3}). The S-NbS$_2$ nanoflakes were produced through the liquid-phase exfoliation (LPE) of 2H/3R-NbS$_2$ crystals followed by functionalization of their surface with mercapto-propane sulfonate molecules. The PEMs were optimized in terms of the S-NbS$_2$ amount in SPEEK with a high DS of 70.2%. Our results demonstrate that the SPEEK/S-NbS$_2$ PEMs with 2.5 wt% of S-NbS$_2$ nanoflakes exhibit excellent dimensional/thermal/chemical stability and selectivity, resulting in VRFBs with EE up to 89.3%, 80.1% and 72.8% at a current density of 100, 200 and 300 mA cm^{-2}, respectively. These metric values are superior to those achieved for VRFBs using PEMs based on pristine SPEEK (e.g., EE of 82.5 and 71.4 at a current density of 100 and 200 mA cm^{-2}). Owing to the efficient proton transporting properties, the VRFBs based on SPEEK/S-NbS$_2$ PEMs can deliver a maximum power density of 0.83 W cm^{-2}. Overall, S-NbS$_2$ nanoflakes are promising additives for the development of advanced nanocomposite PEMs for redox flow battery technologies.

2. Results and discussion

2.1. Characterization of nanoflakes and membranes

Scheme 1 illustrates the functionalization process of the NbS$_2$ nanoflakes. The Fourier-transform infrared (FTIR) spectra of the NbS$_2$ and S-NbS$_2$ nanoflakes are shown in Fig. S1,† proving the successful functionalization of the exfoliated materials. The morphology of the as-produced nanoflakes was investigated by transmission electron microscopy (TEM) and atomic
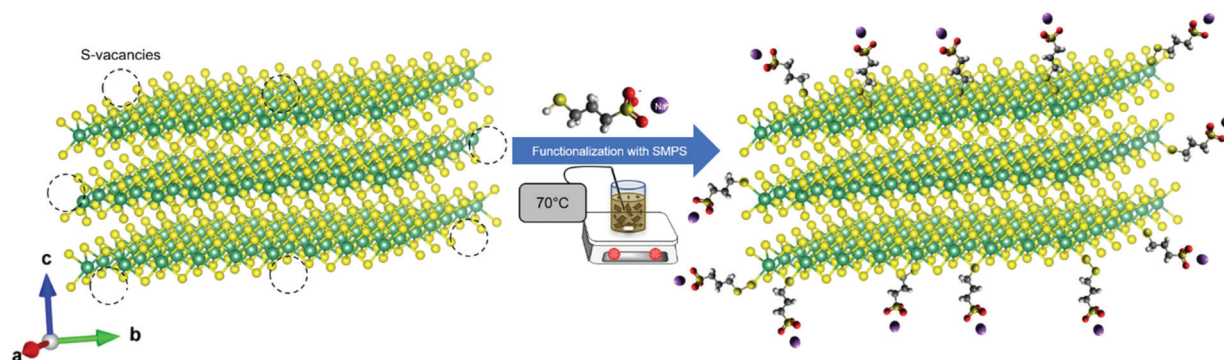
Scheme 1 Sketch of the functionalization of NbS$_2$ nanoflakes,[74] showing the linking of the thiol group of the SMPS molecules to the NbS$_2$ surface *via* S−S bonding or S−vacancy passivation.
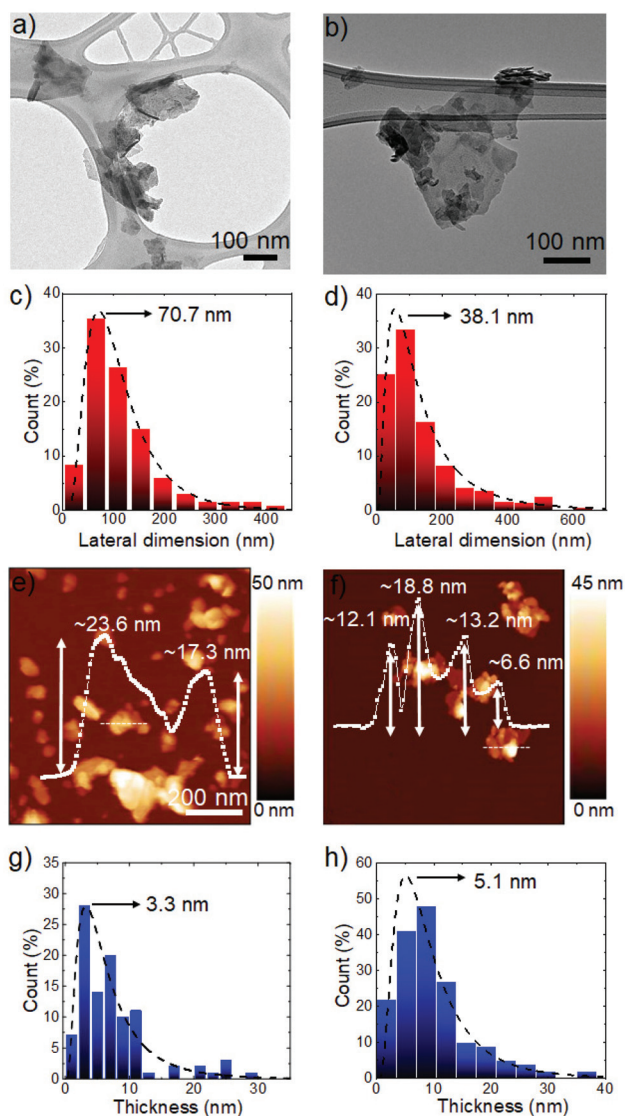

Fig. 1 (a and b) BF-TEM images and (c and d) lateral dimension statistical analyses of the NbS$_2$ and S-NbS$_2$ nanoflakes, respectively. (e and f) AFM images and (g and h) thickness statistical analyses of the NbS$_2$ and S-NbS$_2$ nanoflakes, respectively.

force microscopy (AFM) measurements. Fig. 1a and b show the BF-TEM images of the representative NbS$_2$ and S-NbS$_2$ nanoflakes, respectively, which display the nearly same morphology, *i.e.*, wrinkled surfaces with irregular shapes and sharp edges. Fig. 1c and d show that the lateral size data follow a log–normal distribution peaking at ~70.7 nm, with maximum values above 400 nm, and ~38.1 nm, with maximum values above 600 nm, for NbS$_2$ and S-NbS$_2$ nanoflakes, respectively. Fig. 1e and f show the AFM images of the representative NbS$_2$ and S-NbS$_2$ nanoflakes, respectively, whose height profiles reveal the presence of few-/multi-layer flakes (measured AFM thicknesses of NbS$_2$ monolayers are between 0.6 nm and 0.9 nm, depending on the substrate).[72,73] Meanwhile, the log–normal distribution fitting the AFM thickness data peaks at ~3.3 nm and ~5.1 nm for NbS$_2$ and S-NbS$_2$ nanoflakes, respectively (Fig. 1g and h), with minimum values corresponding to the monolayers (<1 nm). Overall, the morphology of the functionalized nanoflakes is still similar to that of the native NbS$_2$ nanoflakes.

The S-NbS$_2$ crystal structure was evaluated by X-ray diffraction (XRD) and Raman spectroscopy. Fig. 2a shows the XRD pattern obtained for the S-NbS$_2$ nanoflakes, together with those of the native NbS$_2$ bulk crystals and NbS$_2$ nanoflakes. The NbS$_2$ crystals are indexed with the PDF card no. 04-005-8447 for the hexagonal phase of 2H-NbS$_2$ (space group: $P6_3/mmc$)[75,76] and 04-004-7343 for the hexagonal phase of 3R-NbS$_2$
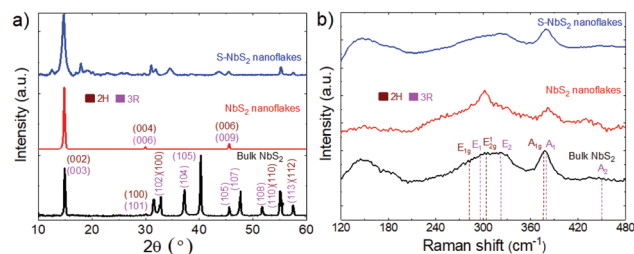

Fig. 2 (a) XRD patterns and (b) Raman spectra of the NbS$_2$ bulk crystals and the exfoliated NbS$_2$ and S-NbS$_2$ nanoflakes. The XRD and Raman peaks assigned to the 2H- and 3R-NbS$_2$ phases are also shown.

(space group: $R3m$).[75,77] The (002) peak of the exfoliated nano-flakes is broader (full width half maximum (FWHM) = 0.27° and 0.64° for NbS$_2$ and S-NbS$_2$, respectively) than that of the NbS$_2$ bulk crystals (FWHM = 0.24°), due to the reduced crystalline domains of the NbS$_2$ nanoflakes. The other peaks are strongly reduced in intensity although retaining their original positions, indicating that the NbS$_2$ nanoflakes preserve their crystal structure.[78] Although some extra XRD peaks are observed in the S-NbS$_2$ nanoflakes, their positions do not match with those of niobium oxide, suggesting that the LPE and functionalization processes do not oxidize S-NbS$_2$ nanoflakes.

Fig. 2b shows the Raman spectra of the NbS$_2$ bulk crystals and the exfoliated NbS$_2$ and S-NbS$_2$ nanoflakes. According to the group theory for the space group of 2H-NbS$_2$[79,80] and 3R-NbS$_2$,[79,81] the materials display non-degenerate Raman active modes. In particular, the 2H-NbS$_2$ phase shows the E_{1g}, E^1_{2g} and A_{1g} modes at ~270, ~305 and ~380 cm^{-1}, respectively,[79,80] while the 3R-NbS$_2$ phase exhibits the E_1, E_2, A_1 and A_2 modes at ~290, ~335, ~385, and ~450 cm^{-1}, respectively.[79,81,82] The bands at wavelengths inferior to 210 cm^{-1} are associated to the two-phonon scattering processes in the presence of defects.[73,77,81] The peaks related to 2H-NbS$_2$ are more pronounced in the exfoliated flakes compared to the bulk crystals, suggesting that the exfoliation process can promote a 3R- to 2H-phase conversion, in agreement with the literature.[51,73] Moreover, the A_2 mode of 3R-NbS$_2$ red-shifts from ~450 cm^{-1} in the NbS$_2$ crystals to ~435 cm^{-1} in the nanoflakes, because the interlayer van der Waals forces relax by decreasing the number of layers.[51,83] Overall, the Raman spectrum of the S-NbS$_2$ nanoflakes indicates that the exfoliation and functionalization processes do not significantly change the crystalline structure of the bulk crystals.

The cross-sectional morphology of the PEMs and the distribution of the S-NbS$_2$ nanoflakes within the SPEEK matrices were evaluated by X-ray spectroscopy (EDX)-coupled scanning electron microscopy (SEM) measurements. Fig. 3a and b show the cross-sectional SEM images of the SPEEK and SPEEK:2.5% S-NbS$_2$ membranes, respectively. As shown later, the SPEEK:2.5% S-NbS$_2$ membrane exhibited the best performance in terms of selectivity metrics among the investigated membranes. The pristine SPEEK membrane exhibit a porous cross-sectional internal morphology, made of pores with lateral dimensions mainly in the 1–5 μm range (Fig. 3a). This distinctive morphology is associated with the sulfonation process that introduces hydrophilic –SO$_3$H groups causing the reorganization of the hydrophobic backbone formed by SPEEK chains. The nanocomposite membrane shows a fracture surface rougher than that the SPEEK membrane. The structure is still made of crack-free domains, whose dimensions are reduced compared to those of SPEEK likely because of spatial constraints imposed by the S-NbS$_2$ nanoflakes. Similar effects have been previously observed in membranes based on SPEEK and 2D materials as additives.[18,84] The absence of aggregated S-NbS$_2$ nanoflakes indicates that the polymeric matrix opti-
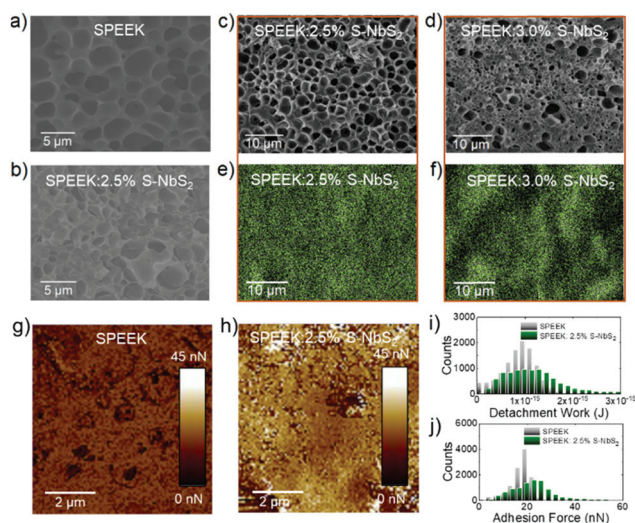

Fig. 3 Cross-sectional SEM images of the (a) SPEEK and (b) SPEEK:2.5% S-NbS$_2$ membranes. Back-scattered and secondary electron images of the (c) SPEEK:2.5% S-NbS$_2$ and (d) SPEEK:3.0% S-NbS$_2$ membranes. EDX maps of the (e) SPEEK:2.5% S-NbS$_2$ and (f) SPEEK:3.0% S-NbS$_2$ membranes for Nb (M line at 2.18 keV). (g and h) Adhesion force maps measured by AFM for the SPEEK and SPEEK:2.5% S-NbS$_2$ membranes in humid ambient air, respectively, and the corresponding (i) detachment work and (j) adhesion force distributions.

mally surrounds the nanoflakes without creating voids (*e.g.*, mesopores). These results confirm the chemical compatibility between S-NbS$_2$ and SPEEK,[85] which originates from the hydrogen bonds between the functionalized groups of the S-NbS$_2$ nanoflakes and the sulfonated groups of SPEEK.[18]

The EDX maps of Nb in the SPEEK:2.5% S-NbS$_2$ membrane, corresponding to the SEM image reported in Fig. 3c, are shown in Fig. 3e. These results confirm further that the S-NbS$_2$ nanoflakes are homogeneously dispersed in the SPEEK matrix. However, by increasing the content of the S-NbS$_2$ nanoflakes up to 3 wt%, significant nanoflakes agglomeration occurs (Fig. 3f corresponds to the SEM image reported in Fig. 3d), resulting in an inhomogeneous membrane structure.[42] The aggregation of S-NbS$_2$ nanoflakes can provide vacant sites for vanadium ion penetration, which can negatively affect the CE of the corresponding VRFBs, as confirmed by our electrochemical analysis shown later in the text.[86] Atomic force measurements were carried out to assess the different membrane hydrophobic–hydrophilic nanophase separation, which is correlated to the membrane adhesion properties in humid ambient air (relative humidity (RH) ~75%).[87–89] According to the Lennard-Jones force–separation relation,[90,91] adhesion force measurements can distinguish the water accessible sites of membranes, which are typically expressed by hydrophilic porous nano/microphases.[87–89] More in detail, in humid air, the adhesion forces between the membrane and the AFM tip are determined by capillary forces,[92] which rely on the hydrophilicity/hydrophobicity of the membrane.[87,88] In addition, the chemical specificity (*e.g.*, the presence of functional groups) of the membranes can also affect the pull-off force,[93,94] providing

quantitative information regarding the existence of hydrophilic polar chemical species.

Fig. 3g and h show the adhesion force maps measured for SPEEK and SPEEK:2.5% S-NbS$_2$, respectively. The corresponding detachment work (*i.e.*, work needed to detach the AFM tip from the sample) and adhesion force distributions are shown in Fig. 3i and j, respectively. The mean detachment work values are $(0.89 \pm 0.37) \times 10^{-15}$ J and $(1.14 \pm 0.02) \times 10^{-15}$ J for SPEEK and SPEEK:2.5% S-NbS$_2$, respectively. These values correspond to a mean adhesion force of 17.5 ± 4.4 nN and 22.5 ± 9.1 nN, respectively. These data indicate that SPEEK:2.5% S-NbS$_2$ exhibits more hydrophilic domains and polar functional groups compared to SPEEK. These chemical characteristics are correlated to the high WU of SPEEK:2.5% S-NbS$_2$, which results in high σ, in agreement with previous characterization studies.

2.2. Physicochemical properties

The WU and MS of the investigated membranes are shown in Fig. 4. The WU results of the pristine SPEEK, SPEEK:1.5% S-NbS$_2$, SPEEK:2.0% S-NbS$_2$, SPEEK:2.5% S-NbS$_2$ and SPEEK:3.0% S-NbS$_2$ membranes are 37.4%, 38.0%, 39.8%, 40.4% and 40.1%, respectively. The incorporation of the S-NbS$_2$ nanoflakes into the SPEEK slightly increases the WU of the nanocomposite membranes. This effect can be explained by the interaction of the water molecules with the hydrophilic groups of the S-NbS$_2$ nanoflakes. The addition of more than 2.5 wt% of the S-NbS$_2$ nanoflakes into the SPEEK causes a slight decrease in WU. In fact, the S-NbS$_2$ nanoflake aggregation, as confirmed by EDX analysis (see Fig. 3f), can cause the closure of the available transport channels in the membrane. However, the nanocomposite membranes show MS significantly lower than that of the pristine SPEEK membrane (15.3%). In particular, the MS of the membranes clearly decreases by increasing the wt% of the S-NbS$_2$ nanoflakes, reaching a minimum value of 7.5% for the SPEEK:3.0% S-NbS$_2$ 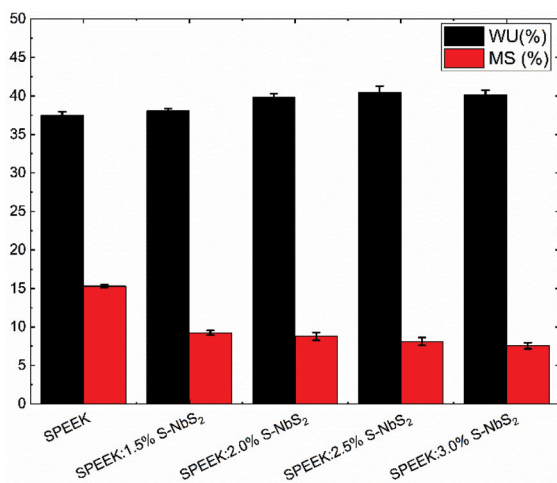membrane. This phenomenon can be attributed to the more compact structure of the membrane in the presence of strong hydrogen bonds between the functionalized groups of S-NbS$_2$ nanoflakes and the polymer, which can prevent membrane size change.[95] The decrease of MS can be directly associated with an improvement of the dimensional stability, which is desirable for a long-term VRFB operation without performance fade.[96]

The σ of the membranes is another crucial metric for their use in high-VE VRFBs.[97] The measured σ values of the produced membranes at room temperature are shown in Table 1. The σ values of the pristine SPEEK, SPEEK:1.5% S-NbS$_2$, SPEEK:2.0% S-NbS$_2$, SPEEK:2.5% S-NbS$_2$, and SPEEK:3.0% S-NbS$_2$ membranes were 45.82, 79.12, 89.17, 94.35 and 85.88 mS cm^{-1}, respectively. Clearly, the σ value of the nanocomposite membranes increases with increasing wt% of the S-NbS$_2$ nanoflakes, until reaching the maximum value of 2.5 wt%. The higher σ value of the nanocomposite membranes compared to the pristine SPEEK membrane has a two-fold origin. First, the functional groups of the S-NbS$_2$ nanoflakes interact with the sulfonate groups of SPEEK, creating efficient proton transport pathways *via* the Grotthuss mechanism.[98–100] Second, the hydrophilic properties of the S-NbS$_2$ nanoflakes improve the retention of water molecules, which host and transport the protons *via* the vehicle mechanism.[101] The SPEEK:2.5% S-NbS$_2$ membrane shows a higher σ value (94.35 mS cm^{-1}) compared to the SPEEK:3.0% S-NbS$_2$ membrane (85.88 mS cm^{-1}) because an excess amount of S-NbS$_2$ nanoflakes cause the formation of aggregates that can block the continuity of the proton transport channels.[102]

P is another valuable metric of PEMs that significantly influences both selectivity and long-term cycling stability of VRFBs.[103] The P values measured for the investigated membranes are reported in Table 1. Generally, SPEEK-based membranes show low P due to their low hydrophilic/hydrophobic nanophase separation, which results from the connection of the hydrophobic backbone to hydrophilic branches.[23] By increasing the loading of the S-NbS$_2$ nanoflakes into the polymeric matrix, the P value first decreases from 5.42×10^{-7} cm^2 min^{-1} in the pristine SPEEK membrane to 2.34×10^{-7} cm^2 min^{-1} in the SPEEK:2.5% S-NbS$_2$ membrane, and then increases to 2.83×10^{-7} cm^2 min^{-1} in the SPEEK:3.0% S-NbS$_2$ membrane. The obtained results reveal that the ability to block the penetration of VO^{2+} of the nanocomposite membranes is superior to that of the pristine SPEEK membrane. By

Fig. 4 The WU and MS values of the investigated membranes.

Table 1 Membrane parameter (σ, P, selectivity and weight loss) values measured for the investigated membranes at room temperature

Membrane	σ (mS cm^{-1})	P (cm^2 min^{-1})	Selectivity (S min cm^{-3})	Weight loss (%)
SPEEK	45.82	5.42×10^{-7}	8.45×10^{4}	5.94
SPEEK:1.5% S-NbS$_2$	79.12	3.14×10^{-7}	25.19×10^{4}	4.68
SPEEK:2.0% S-NbS$_2$	89.17	2.53×10^{-7}	35.24×10^{4}	4.12
SPEEK:2.5% S-NbS$_2$	94.35	2.34×10^{-7}	40.32×10^{4}	3.87
SPEEK:3.0% S-NbS$_2$	85.88	2.83×10^{-7}	30.34×10^{4}	3.71

increasing S-NbS$_2$ content up to 2.5 wt%, the nanocomposite membranes show compact structures and low MS (7.9%) due to the interaction of the functionalized groups of S-NbS$_2$ nanoflakes and SPEEK, leading to a decrease in P. By increasing the S-NbS$_2$ nanoflake content above 2.5 wt%, P increases due to the aggregation of the S-NbS$_2$ nanoflakes in the structure (see Fig. 3f), altering the compactness of the membrane structure and facilitating the permeation of VO^{2+}.[61] The compactness of the structures could in principle squeezes the proton transport channels. However, as supported by our σ data, the sulfonate groups of the S-NbS$_2$ nanoflakes represent proton hopping sites that enhance the σ via the Grotthuss mechanism.[104] Therefore, the concomitant engineering of structural and chemical properties allows the dichotomy of the behavior of membrane performance to be managed. In this context, selectivity is a comprehensive factor to predict the performance of the produced membrane in VRFBs.[105] As shown in Table 1, the selectivity of the nanocomposite membranes is superior to that of the pristine SPEEK membrane. Specifically, the selectivity increases from 8.45×10^4 S min cm^{-3} in the SPEEK membrane up to 40.32×10^4 S min cm^{-3} in the SPEEK:2.5% S-NbS$_2$ membrane. Overall, the SPEEK:2.5% S-NbS$_2$ membrane exhibits the best physicochemical properties among the investigated membranes to be used in VRFB applications.

To study the chemical stability of the membranes under strong acidic and oxidizing conditions, the weight losses of the membranes in a 1.5 M VO$_2^+$ + 3 M H$_2$SO$_4$ solution after 30 days were measured, and the data are presented in Table 1. The SPEEK membrane shows the highest weight loss (5.94%) among the produced membranes, which is mainly related to the decomposition of the PEEK backbone in the presence of the oxidizing VO^{2+}.[106] The weight loss percentage of the nanocomposite membranes decreases from 4.68% to 3.71% by increasing the S-NbS$_2$ amount from 1.5 to 3.0 wt%. These results indicate that the strong hydrogen bonds formed between the functionalized groups of S-NbS$_2$ and SPEEK can passivate the degradation process of the polymer backbone, thus improving the chemical stability of the pure SPEEK membrane.[18] As shown in Fig. S2 and Table S1,† the produced PEMs were further characterized in terms of ion exchange capacity (IEC) and mechanical and thermal stabilities by performing a conventional acid–base titration experiment, tensile test and thermogravimetric analysis, respectively. The obtained results confirm the improvement of the membrane performances upon the incorporation of the S-NbS$_2$ nanoflakes.

2.3. Evaluation of the performances of VRFBs

The performances of the membranes were evaluated in VRFBs using a no-gap serpentine architecture[107,108] and plasma-treated graphite felt as the electrodes,[109] and 1 M VO^{2+} + 3 M H$_2$SO$_4$ and 1 M V^{3+} + 3 M H$_2$SO$_4$ as the starting catholyte (positive electrolyte) and anolyte (negative electrolyte), respectively. A VRFB based on commercially viable Nafion 115 was also test for comparison. Hereafter, the VRFBs are indicated with the name of their membranes. Fig. 5a shows the polarization
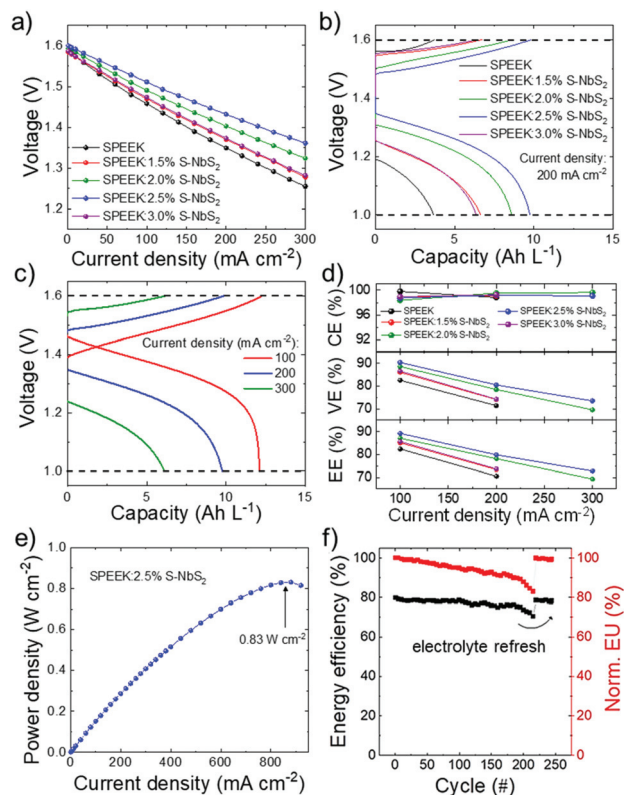

Fig. 5 (a) Polarization curves and (b) charge/discharge curves measured for the investigated VRFBs (SPEEK, SPEEK:1.5% S-NbS$_2$, SPEEK:2.0% S-NbS$_2$, SPEEK:2.5% S-NbS$_2$ and SPEEK:3.0% S-NbS$_2$). (c) Charge/discharge curves measured for the SPEEK:2.5% S-NbS$_2$ membrane at current densities of 100, 200 and 300 mA cm^{-2}. (d) Efficiency metrics (CE, VE and EE) for the VRFBs using the SPEEK and SPEEK:x% S-NbS$_2$ membranes as a function of the cycle number at different current densities (data extrapolated from the CD curve analysis). (e) Power density as a function of the discharge current density measured for the SPEEK:2.5% S-NbS$_2$ membrane. (f) Long-term stability tests for the SPEEK:2.5% S-NbS$_2$ membrane cycled at a current density of 200 mA cm^{-2}. Left y-axis: energy efficiency; right y-axis: normalized electrolyte utilization (Norm. EU).

curves measured for the investigated VRFBs. These data evidence the different ohmic (iR) losses attributed to the resistance of the PEM, since the kinetic losses resulting from the catalytic activity of the electrodes toward the VRFB redox reactions are similar for all VRFBs, which use the same type of electrodes.[110,111] Clearly, the SPEEK:2.5% S-NbS$_2$ membrane shows the lowest polarization losses, corresponding to 0.089 V, 0.168 V and 0.239 V at current densities of 100, 200 and 300 mA cm^{-2}. Moreover, all the nanocomposite membranes led to lower iR losses compared to the SPEEK membrane, because of their higher σ, as shown in Table 1. Galvanostatic charge/discharge (CD) analysis was carried out to evaluate the efficiency metrics of the VRFBs, *i.e.*, CE, VE and EE. The upper voltage limit was fixed to 1.6 V in order to avoid parasitic reactions (*i.e.*, water splitting reactions), as recommended in the literature.[112] Fig. 5b shows the charge/discharge curves of the VRFBs assembled with the different produced membranes at a

current density of 200 mA cm^{-2}. The SPEEK:2.5% S-NbS$_2$ membrane shows the highest discharge capacity (9.7 A h L^{-1}), proving the superior balance between σ and P of this nanocomposite membrane. According to the calculated selectivity of the synthesized membranes, the discharge capacity of the corresponding VRFBs decreases with the following order: SPEEK:2.5% S-NbS$_2$ > SPEEK:2.0% S-NbS$_2$ > SPEEK:3.0% S-NbS$_2$ > SPEEK:1.5% S-NbS$_2$ > SPEEK. Fig. 5c shows the charge/discharge curves of the SPEEK:2.5% S-NbS$_2$ membrane at different current densities, ranging from 100 to 300 mA cm^{-2}. The discharge capacity increases by decreasing the current density because of the reduced polarization losses, in agreement with polarization curves (Fig. 5a). At 100 mA cm^{-2}, the discharge capacity is as high as 12.1 A h L^{-1}, corresponding to an electrolyte utilization of 90.6%. At the highest current density of 300 mA cm^{-2}, the SPEEK:2.5% S-NbS$_2$ membrane can still deliver a discharge capacity of approximately 6.5 A h L^{-1}.

Fig. 5d shows the efficiency metrics (*i.e.*, CE, VE and EE) as a function of the current density. The CE value of the nanocomposite membranes is in the range of 98.4–99.8% in the current density range of 100–300 mA cm^{-2}. The increase of the CE value with increasing the current density is related to the decrease of charge–discharge time, minimizing the capacity loss.[18] In addition, the CE values are comparable to those measured for pristine SPEEK. Importantly, the high CE values (*i.e.*, >98%) measured for the investigated VRFBs indicate a limited cross-mixing of vanadium species, avoiding anolyte losses and modifications of the electrolytes' compositions during the cycling of the VRFBs.[113–116] At 100 mA cm^{-2}, the VE values of the pristine SPEEK, SPEEK:1.5% S-NbS$_2$, SPEEK:2.0% S-NbS$_2$, SPEEK:2.5% S-NbS$_2$ and SPEEK:3.0% S-NbS$_2$ membranes are 82.5%, 86.2%, 88.4%, 90.2% and 86.5%, respectively. The VE value of the produced membranes initially increases from 82.5% to 90.2% with increasing S-NbS$_2$ nanoflakes content up to 2.5 wt% S-NbS$_2$, following the same trend of σ. Additionally, SPEEK:2.5% S-NbS$_2$ shows the highest EE values, *e.g.*, 89.3% at a current density of 100 mA cm^{-2}, which is significantly superior to the EE value of SPEEK, *i.e.*, 82.5%. These results confirm the optimal balance between σ and P of the optimized membranes, proving the potential of S-NbS$_2$ nanoflakes as 2D additives for the realization of high-selective membranes. By benefiting from the high σ value, the SPEEK:2.5% S-NbS$_2$ membrane can deliver a maximum power density as high as 0.83 W cm^{-2} at the current density of 870 mA cm^{-2} (Fig. 5e). Table S2† compares the CE, VE and EE values achieved by our work with those reported in literature for other VRFBs based on Nafion (including our Nafion 115-based VRFB reference) and other SPEEK-based membranes. Owing to the excellent selectivity of our nanocomposite membranes, our VRFBs outperform most of the systems reported in literature, including our Nafion 115-based VRFB membrane (CE, VE and EE at 100 mA cm^{-2} of 98%, 86.9% and 85.2%). At the current density of 100 mA cm^{-2}, our nanocomposite membrane significantly increases the EE value of our Nafion 115-based VRFB by almost 5% because of the superior selectivity of our nanocomposite membrane. Self-discharge measurements confirmed the lower P value (leading to a superior selectivity) of our nanocomposite membranes compared to that of Nafion 115 (Fig. S3†), showing discharge times of 76.3 h and 37.8 h for SPEEK:2.5% S-NbS$_2$ and Nafion 115, respectively.

Long-term cycling tests were performed to evaluate the stability of the SPEEK:2.5% S-NbS$_2$ nanocomposite membrane under VRFB operation. As shown in Fig. 5f, the SPEEK:2.5% S-NbS$_2$ membrane shows a stable EE value over the first 100 cycles, together with a slow fade (~−0.05%/cycle over the first 100 cycles) of electrolyte utilization. The EE fading of the VRFB after 200 cycles is related to the asymmetric transfer of various ions and water across the membrane (which are, however, mitigated by our membrane, in agreement with our CE analysis), as well as the infiltration of air in the anolyte, leading to the oxidation of the V^{2+} ion.[12,117] As shown in Fig. 5f, the EE value of the SPEEK:2.5% S-NbS$_2$ returned to the initial EE value after refreshing the electrolyte. These results confirm that the physical and chemical structure of the membrane is preserved under acidic and oxidation conditions. Overall, the electrochemical VRFB characterization indicates that the use of the S-NbS$_2$ nanoflakes as 2D additives of the SPEEK membrane significantly improves the final performance of the VRFBs. The excellent performance of the SPEEK:2.5% S-NbS$_2$ nanocomposite membrane demonstrates that the S-NbS$_2$ nanoflakes act both as proton conductors and VO^{2+} barriers in the nanocomposite membrane, demonstrating the potential of S-NbS$_2$ nanoflakes as 2D additives for PEMs.

3. Conclusions

In summary, sulfonated poly(ether ether ketone) (SPEEK)/sulfonated niobium disulphide (S-NbS$_2$) nanocomposite membranes were produced *via* a solution casting method as promising proton-exchange membranes (PEMs) for vanadium redox flow battery (VRFB) applications. Two-dimensional (2D) NbS$_2$ nanoflakes were synthesized *via* liquid-phase exfoliation (LPE) of bulk NbS$_2$ crystals and functionalized with sodium 3-mercapto-1-propane sulfonate salt (SMPS) molecules. The use of S-NbS$_2$ nanoflakes as an additive improves the SPEEK proton conductivity (σ) from 45.82 to 94.35 mS cm^{-2} in the SPEEK:2.5% S-NbS$_2$ membrane. Additionally, the produced S-NbS$_2$ nanoflakes compact the membrane structure by forming hydrogen bonds between the sulfonated groups of the nanoflakes and SPEEK chains, resulting in effective physical barriers against the diffusion of the vanadium species. By studying the morphological properties of the produced membranes, the optimal content of the S-NbS$_2$ nanoflakes was found to be 2.5 wt%. By further increasing the content of S-NbS$_2$ nanoflakes up to 3 wt%, the structure of the membrane is altered because of the formation of aggregates, decreasing both σ and selectivity. The VRFBs using the optimized membrane (SPEEK:2.5% S-NbS$_2$) achieve an energy efficiency (EE) of 89.3% at a current density of 100 mA cm^{-2}. At the highest current density of 300 mA cm^{-2}, the VRFB exhibits an EE of

72.8% and still delivers a discharge capacity of 6.5 A h L^{-1}. Additionally, the cycling stability of the produced SPEEK:2.5% S-NbS$_2$ nanocomposite membrane in the VRFB is validated over more than 200 cycles of continuous operation at a current density of 200 mA cm^{-2}. The obtained results demonstrate the potentiality of the SPEEK:2.5% S-NbS$_2$ nanocomposite membrane for VRFB applications.

Author contributions

Conflicts of interest

There are no conflicts to declare.

Acknowledgements

Notes and references

1 A. W. Lantz, S. A. Shavalier, W. Schroeder and P. G. Rasmussen, *ACS Appl. Energy Mater.*, 2019, **2**, 7893–7902.

2 F.-C. Gu, H.-C. Chen and K.-Y. Li, *Energy Fuels*, 2020, **34**, 10142–10147.

3 H. Beydaghi, S. Abouali, S. B. Thorat, A. E. Del Rio Castillo, S. Bellani, S. Lauciello, S. Gentiluomo, V. Pellegrini and F. Bonaccorso, *RSC Adv.*, 2021, **11**, 35051–35060.

4 D. Heide, M. Greiner, L. von Bremen and C. Hoffmann, *Renewable Energy*, 2011, **36**, 2515–2523.

5 F. Bonaccorso, L. Colombo, G. Yu, M. Stoller, V. Tozzini, A. C. Ferrari, R. S. Ruoff and V. Pellegrini, *Science*, 2015, **347**, 6217.

6 Q. Dai, Z. Liu, L. Huang, C. Wang, Y. Zhao, Q. Fu, A. Zheng, H. Zhang and X. Li, *Nat. Commun.*, 2020, **11**, 13.

7 J. Ren, Y. Dong, J. Dai, H. Hu, Y. Zhu and X. Teng, *J. Membr. Sci.*, 2017, **544**, 186–194.

8 G. L. Soloveichik, *Nature*, 2014, **505**, 163–164.

9 Y. Chen, S. Zhang, J. Jin, C. Liu, Q. Liu and X. Jian, *ACS Appl. Energy Mater.*, 2019, **2**, 8207–8218.

10 X. L. Zhou, T. S. Zhao, L. An, Y. K. Zeng and L. Wei, *J. Power Sources*, 2017, **339**, 1–12.

11 H. Beydaghi, M. Javanbakht, P. Salarizadeh, A. B. Kharepouei and A. A. Zadeh, Nanocomposite blend membrane, *US Patent*, 10873100, 2020.

12 L. Yu, F. Lin, W. Xiao, L. Xu and J. Xi, *Chem. Eng. J.*, 2019, **356**, 622–631.

13 H. Beydaghi, M. Javanbakht, A. Bagheri, H. Ghafarian-Zahmatkesh and K. Hooshyari, *Iran. J. Hydrogen Fuel Cell*, 2017, **4**, 1–11.

14 N. N. Intan, K. Klyukin, T. J. Zimudzi, M. A. Hickner and V. Alexandrov, *J. Power Sources*, 2018, **373**, 150–160.

15 C. Minke and T. Turek, *J. Power Sources*, 2015, **286**, 247–257.

16 B. Jiang, L. Wu, L. Yu, X. Qiu and J. Xi, *J. Membr. Sci.*, 2016, **510**, 18–26.

17 C. A. Machado, G. O. Brown, R. Yang, T. E. Hopkins, J. G. Pribyl and T. H. Epps, *ACS Energy Lett.*, 2021, **6**, 158–176.

18 Y. Zhang, H. Wang, B. Liu, J. Shi, J. Zhang and H. Shi, *J. Mater. Chem. A*, 2019, **7**, 12669–12680.

19 G. Rambabu and S. D. Bhat, *Chem. Eng. J.*, 2014, **243**, 517–525.

20 K. Raja, P. M. Raja and P. M. Ramesh, *Ionics*, 2019, **25**, 5177–5188.

21 J. Kim, Y. Lee, J.-D. Jeon and S.-Y. Kwak, *J. Power Sources*, 2018, **383**, 1–9.

22 Y. Zhang, H. Wang, W. Yu, J. Shi and H. Shi, *J. Membr. Sci.*, 2018, **564**, 916–925.

23 A. Bagheri, P. Salarizadeh, M. Sabooni Asre Hazer, P. Hosseinabadi, S. Kashefi and H. Beydaghi, *Electrochim. Acta*, 2019, **295**, 875–890.

24 J. Xi, Z. Li, L. Yu, B. Yin, L. Wang, L. Liu, X. Qiu and L. Chen, *J. Power Sources*, 2015, **285**, 195–204.

25 J. L. Reyes-Rodriguez, J. Escorihuela, A. García-Bernabé, E. Giménez, O. Solorza-Feria and V. Compañ, *RSC Adv.*, 2017, **7**, 53481–53491.

26 D. Chen, X. Chen, L. Ding and X. Li, *J. Membr. Sci.*, 2018, **553**, 25–31.

27 L. Cao, Q. Sun, Y. Gao, L. Liu and H. Shi, *Electrochim. Acta*, 2015, **158**, 24–34.

28 L. Yu, F. Lin, W. Xiao, D. Luo and J. Xi, *J. Membr. Sci.*, 2018, **549**, 411–419.

29 R. Niu, L. Kong, L. Zheng, H. Wang and H. Shi, *J. Membr. Sci.*, 2017, **525**, 220–228.

30 A. Amoozadeh, H. Mazdarani, H. Beydaghi, E. Tabrizian and M. Javanbakht, *New J. Chem.*, 2018, **42**, 16855–16862.

31 A. Bagheri, M. Javanbakht, P. Hosseinabadi, H. Beydaghi and A. Shabanikia, *Polymer*, 2018, **138**, 275–287.

32 W. Dai, Y. Shen, Z. Li, L. Yu, J. Xi and X. Qiu, *J. Mater. Chem. A*, 2014, **2**, 12423–12432.

33 H. Beydaghi, M. Javanbakht, A. Bagheri, P. Salarizadeh, H. G. Zahmatkesh, S. Kashefi and E. Kowsari, *RSC Adv.*, 2015, **5**, 74054–74064.

34 Z. Li, W. Dai, L. Yu, J. Xi, X. Qiu and L. Chen, *J. Power Sources*, 2014, **257**, 221–229.

35 H. Beydaghi, A. Bagheri, P. Salarizadeh, S. Kashefi, K. Hooshyari, A. Amoozadeh, T. Shamsi, F. Bonaccorso and V. Pellegrini, *Ind. Eng. Chem. Res.*, 2020, **59**, 6589–6599.

36 T. Roy, S. K. Wanchoo and K. Pal, *Solid State Ionics*, 2020, **349**, 115296.

37 K. Hooshyari, S. Heydari, M. Javanbakht, H. Beydaghi and M. Enhessari, *RSC Adv.*, 2020, **10**, 2709–2721.

38 X. Yan, H. Zhang, Z. Hu, L. Li, L. Hu, Z. Li, L. Gao, Y. Dai, X. Jian and G. He, *ACS Appl. Mater. Interfaces*, 2019, **11**, 44315–44324.

39 W. Wang, M. Xu, S. Wang, X. Xie, Y. Lv and V. K. Ramani, *ACS Appl. Mater. Interfaces*, 2014, DOI: 10.1021/am501540g.

40 J. Kim, J.-D. Jeon and S.-Y. Kwak, *Electrochim. Acta*, 2017, **243**, 220–227.

41 S. Khilari, S. Pandit, M. M. Ghangrekar, D. Pradhan and D. Das, *Ind. Eng. Chem. Res.*, 2013, **52**, 11597–11606.

42 H. Beydaghi and M. Javanbakht, *Ind. Eng. Chem. Res.*, 2015, **54**, 7028–7037.

43 H. Beydaghi, M. Javanbakht and E. Kowsari, *Ind. Eng. Chem. Res.*, 2014, **53**, 16621–16632.

44 K. Feng, B. Tang and P. Wu, *ACS Appl. Mater. Interfaces*, 2013, **5**, 13042–13049.

45 K. Divya, M. S. Sri Abirami Saraswathi, D. Rana, S. Alwarappan and A. Nagendran, *Polymer*, 2018, **147**, 48–55.

46 K. Divya, D. Rana, M. S. Sri Abirami Saraswathi, S. D. Bhat, A. Shukla and A. Nagendran, *Int. J. Hydrogen Energy*, 2020, **45**, 15507–15520.

47 C. Ataca and S. Ciraci, *J. Phys. Chem. C*, 2011, **115**, 13303–13311.

48 S. S. Chou, M. De, J. Kim, S. Byun, C. Dykstra, J. Yu, J. Huang and V. P. Dravid, *J. Am. Chem. Soc.*, 2013, **135**, 4584–4587.

49 S. Bellani, A. Bartolotta, A. Agresti, G. Calogero, G. Grancini, A. Di Carlo, E. Kymakis and F. Bonaccorso, *Chem. Soc. Rev.*, 2021, **50**, 11870–11965.

50 D. Voiry, A. Goswami, R. Kappera, C. de C. C. e Silva, D. Kaplan, T. Fujita, M. Chen, T. Asefa and M. Chhowalla, *Nat. Chem.*, 2015, **7**, 45–49.

51 L. Najafi, S. Bellani, R. Oropesa-Nuñez, B. Martín-García, M. Prato, V. Mazánek, D. Debellis, S. Lauciello, R. Brescia, Z. Sofer and F. Bonaccorso, *J. Mater. Chem. A*, 2019, **7**, 25593–25608.

52 H. Beydaghi, L. Najafi, S. Bellani, A. Bagheri, B. Martín-García, P. Salarizadeh, K. Hooshyari, S. Naderizadeh, M. Serri, L. Pasquale, B. Wu, R. Oropesa-Nuñez, Z. Sofer, V. Pellegrini and F. Bonaccorso, *J. Mater. Chem. A*, 2021, **9**, 6368–6381.

53 L. Najafi, S. Bellani, R. Oropesa-Nuñez, B. Martín-García, M. Prato, L. Pasquale, J.-K. Panda, P. Marvan, Z. Sofer and F. Bonaccorso, *ACS Catal.*, 2020, **10**, 3313–3325.

54 I. Raj, Y. Duan, D. Kigen, W. Yang, L. Hou, F. Yang and Y. Li, *Front. Mater. Sci.*, 2018, **12**, 239–246.

55 Y. Feng, S. Gong, E. Du, X. Chen, R. Qi, K. Yu and Z. Zhu, *J. Phys. Chem. C*, 2018, **122**, 2382–2390.

56 L. Najafi, S. Bellani, R. Oropesa-nuñez, R. Brescia, M. Prato, L. Pasquale, C. Demirci, F. Drago, B. Martín-garcía, J. Luxa, L. Manna, Z. Sofer and F. Bonaccorso, *Small*, 2020, **16**, 2003372.

57 C. Yang, J. Feng, F. Lv, J. Zhou, C. Lin, K. Wang, Y. Zhang, Y. Yang, W. Wang, J. Li and S. Guo, *Adv. Mater.*, 2018, **30**, 1800036.

58 Z. Zhang, J. Niu, P. Yang, Y. Gong, Q. Ji, J. Shi, Q. Fang, S. Jiang, H. Li, X. Zhou, L. Gu, X. Wu and Y. Zhang, *Adv. Mater.*, 2017, **29**, 1702359.

59 S. Ayyaru and S. Dharmalingam, *Energy*, 2015, **88**, 202–208.

60 V. Parthiban, S. Akula and A. K. Sahu, *J. Membr. Sci.*, 2017, **541**, 127–136.

61 M. Wang, G. Liu, X. Cui, Y. Feng, H. Zhang, G. Wang, S. Zhong and Y. Luo, *Solid State Ionics*, 2018, **315**, 71–76.

62 Y. Cui, S. I. Kundalwal and S. Kumar, *Carbon*, 2016, **98**, 313–333.

63 Y. Su, V. G. Kravets, S. L. Wong, J. Waters, A. K. Geim and R. R. Nair, *Nat. Commun.*, 2014, **5**, 4843.

64 S. Kim, J. Choi, C. Choi, J. Heo, D. W. Kim, J. Y. Lee, Y. T. Hong, H.-T. Jung and H.-T. Kim, *Nano Lett.*, 2018, **18**, 3962–3968.

65 L. Zhang, L. Ling, M. Xiao, D. Han, S. Wang and Y. Meng, *J. Power Sources*, 2017, **352**, 111–117.

66 K. Ngamsai and A. Arpornwichanop, *J. Power Sources*, 2015, **295**, 292–298.

67 Y.-C. Cao, C. Xu, X. Wu, X. Wang, L. Xing and K. Scott, *J. Power Sources*, 2011, **196**, 8377–8382.

68 Z. Li, J. Xi, H. Zhou, L. Liu, Z. Wu, X. Qiu and L. Chen, *J. Power Sources*, 2013, **237**, 132–140.

69 H. Beydaghi, M. Javanbakht, P. Salarizadeh, A. Bagheri and A. Amoozadeh, *Polymer*, 2017, **119**, 253–262.

70 Q. Tan, S. Lu, J. Si, H. Wang, C. Wu, X. Li and Y. Xiang, *Macromol. Rapid Commun.*, 2017, **38**, 1600710.

71 S.-H. Yang, D.-S. Yang, S. J. Yoon, S. So, S.-K. Hong, D. M. Yu and Y. T. Hong, *Energy Fuels*, 2020, **34**, 7631–7638.

72 S. Zhao, T. Hotta, T. Koretsune, K. Watanabe, T. Taniguchi, K. Sugawara, T. Takahashi, H. Shinohara and R. Kitaura, *2D Mater.*, 2016, **3**, 025027.

73 X. Wang, J. Lin, Y. Zhu, C. Luo, K. Suenaga, C. Cai and L. Xie, *Nanoscale*, 2017, **9**, 16607–16611.

74 *2H-NbS$_2$ (NbS$_2$ ht) Crystal Structure: Datasheet from "PAULING FILE Multinaries Edition – 2012"*, ed. P. Villars and K. Cenzual, SpringerMaterials (https://materials.springer.com/isp/crystallographic/docs/sd_0547970), 2012.

75 Y. Liao, K.-S. Park, P. Singh, W. Li and J. B. Goodenough, *J. Power Sources*, 2014, **245**, 27–32.

76 Y. Liao, K.-S. Park, P. Xiao, G. Henkelman, W. Li and J. B. Goodenough, *Chem. Mater.*, 2013, **25**, 1699–1705.

77 W. Ge, K. Kawahara, M. Tsuji and H. Ago, *Nanoscale*, 2013, **5**, 5773–5778.

78 L. Najafi, S. Bellani, B. Martín-García, R. Oropesa-Nuñez, A. E. Del Rio Castillo, M. Prato, I. Moreels and F. Bonaccorso, *Chem. Mater.*, 2017, **29**, 5782–5786.

79 W. G. McMullan and J. C. Irwin, *Solid State Commun.*, 1983, **45**, 557–560.

80 S. Nakashima, Y. Tokuda, A. Mitsuishi, R. Aoki and Y. Hamaue, *Solid State Commun.*, 1982, **42**, 601–604.

81 S. Onari, T. Arai, R. Aoki and S. Nakamura, *Solid State Commun.*, 1979, **31**, 577–579.

82 D. Gopalakrishnan, A. Lee, N. K. Thangavel and L. M. Reddy Arava, *Sustainable Energy Fuels*, 2018, **2**, 96–102.

83 J. K. Dash, L. Chen, P. H. Dinolfo, T.-M. Lu and G.-C. Wang, *J. Phys. Chem. C*, 2015, **119**, 19763–19771.

84 Z. Jiang, X. Zhao and A. Manthiram, *Int. J. Hydrogen Energy*, 2013, **38**, 5875–5884.

85 E. Yan, J. Wang, Z. Jiang, H. Feng, L. Nie, T. Xu, X. Yang and X. Zhang, *J. Mater. Chem. A*, 2013, **1**, 11762–11777.

86 X. Li, H. Zhang, Z. Mai, H. Zhang and I. Vankelecom, *Energy Environ. Sci.*, 2011, **4**, 1147–1160.

87 M. Farshchi-Tabrizia, M. Kappl and H.-J. Butt, *J. Adhes. Sci. Technol.*, 2008, **22**, 181–203.

88 L. Najafi, R. Oropesa-Nuñez, B. Martín-García, F. Drago, M. Prato, V. Pellegrini, F. Bonaccorso and S. Bellani, *Mater. Adv.*, 2020, **1**, 387–402.

89 L. Vannozzi, L. Ricotti, T. Santaniello, T. Terencio, R. Oropesa-Nunez, C. Canale, F. Borghi, A. Menciassi, C. Lenardi and I. Gerges, *J. Mech. Behav. Biomed. Mater.*, 2017, **75**, 147–159.

90 J. E. Lennard-Jones, *Proc. Phys. Soc.*, 1931, **43**, 461–482.

91 N. Yu and A. A. Polycarpou, *J. Colloid Interface Sci.*, 2004, **278**, 428–435.

92 D. L. Sedin and K. L. Rowlen, *Anal. Chem.*, 2000, **72**, 2183–2189.

93 E. W. van der Vegte and G. Hadziioannou, *Langmuir*, 1997, **13**, 4357–4368.

94 C. D. Frisbie, L. F. Rozsnyai, A. Noy, M. S. Wrighton and C. M. Lieber, *Science*, 1994, **265**, 2071–2074.

95 M. Ionita, M. A. Pandele and H. Iovu, *Carbohydr. Polym.*, 2013, **94**, 339–344.

96 D. Chen, M. A. Hickner, E. Agar and E. C. Kumbur, *ACS Appl. Mater. Interfaces*, 2013, **5**, 7559–7566.

97 S. Kim, S. Yuk, H. G. Kim, C. Choi, R. Kim, J. Y. Lee, Y. T. Hong and H.-T. Kim, *J. Mater. Chem. A*, 2017, **5**, 17279–17286.

98 K. Ketpang, B. Son, D. Lee and S. Shanmugam, *J. Membr. Sci.*, 2015, **488**, 154–165.

99 M. A. Aziz and S. Shanmugam, *J. Mater. Chem. A*, 2018, **6**, 17740–17750.

100 S. I. Hossain, M. A. Aziz, D. Han, P. Selvam and S. Shanmugam, *J. Mater. Chem. A*, 2018, **6**, 20205–20213.

101 Y. Heo, H. Im and J. Kim, *J. Membr. Sci.*, 2013, **425–426**, 11–22.

102 M. A. Aziz and S. Shanmugam, *J. Mater. Chem. A*, 2017, **5**, 16663–16671.

103 Y. Zhang, H. Wang, W. Yu and H. Shi, *ChemistrySelect*, 2018, **3**, 9249–9258.

104 H. Beydaghi, M. Javanbakht and E. Kowsari, *Polymer*, 2016, **87**, 26–37.

105 Y. Quan, G. Wang, A. Li, X. Wei, F. Li, J. Zhang, J. Chen and R. Wang, *RSC Adv.*, 2019, **9**, 3838–3846.

106 Z. Yuan, X. Li, J. Hu, W. Xu, J. Cao and H. Zhang, *Phys. Chem. Chem. Phys.*, 2014, **16**, 19841–19847.

107 D. S. Aaron, Q. Liu, Z. Tang, G. M. Grim, A. B. Papandrew, A. Turhan, T. A. Zawodzinski and M. M. Mench, *J. Power Sources*, 2012, **206**, 450–453.

108 Q. H. Liu, G. M. Grim, A. B. Papandrew, A. Turhan, T. A. Zawodzinski and M. M. Mench, *J. Electrochem. Soc.*, 2012, **159**, A1246–A1252.

109 S. Bellani, L. Najafi, M. Prato, R. Oropesa-Nuñez, B. Martín-García, L. Gagliani, E. Mantero, L. Marasco, G. Bianca, M. I. Zappia, C. Demirci, S. Olivotto, G. Mariucci, V. Pellegrini, M. Schiavetti and F. Bonaccorso, *Chem. Mater.*, 2021, **33**, 4106–4121.

110 D. Aaron, C.-N. Sun, M. Bright, A. B. Papandrew, M. M. Mench and T. A. Zawodzinski, *ECS Electrochem. Lett.*, 2013, **2**, A29–A31.

111 D. Aaron, Z. Tang, A. B. Papandrew and T. A. Zawodzinski, *J. Appl. Electrochem.*, 2011, **41**, 1175.

112 L. Wu, J. Wang, Y. Shen, L. Liu and J. Xi, *Phys. Chem. Chem. Phys.*, 2017, **19**, 14708–14717.

113 L. Yu, F. Lin, L. Xu and J. Xi, *RSC Adv.*, 2017, **7**, 31164–31172.

114 B. Jiang, L. Yu, L. Wu, D. Mu, L. Liu, J. Xi and X. Qiu, *ACS Appl. Mater. Interfaces*, 2016, **8**, 12228–12238.

115 P. Majsztrik, A. Bocarsly and J. Benziger, *J. Phys. Chem. B*, 2008, **112**, 16280–16289.

116 Q. Duan, H. Wang and J. Benziger, *J. Membr. Sci.*, 2012, **392–393**, 88–94.

117 Y. Liu, L. Yu, L. Liu and J. Xi, *Appl. Energy*, 2021, **301**, 117454.